

Coherent control of pump-probe signals of helical structures by adaptive pulse polarizations

Dmitri Voronine, Darius Abramavicius, and Shaul Mukamel^{a)}*Department of Chemistry, University of California, Irvine, California 92697-2025*

(Received 1 August 2005; accepted 13 September 2005; published online 17 January 2006)

The simplification of the pump-probe spectrum of excitons by pure-phase-polarization pulse shaping is investigated by a simulation study. The state of light is manipulated by varying the phases of two perpendicular polarization components of the pump, holding its total spectral and temporal intensity profiles fixed. Genetic and iterative Fourier transform algorithms are used to search for pulse phase functions that optimize the ratio of the signal at two frequencies. New features are extracted from the congested pump-probe spectrum of a helical pentamer by selecting a combination of Liouville space pathways. Tensor components which dominate the optimized spectra are identified. © 2006 American Institute of Physics. [DOI: 10.1063/1.2107667]

I. INTRODUCTION

Multiple sequences of optical pulses with variable delays provide direct probes for electronic and vibrational motions.^{1–3} Dynamical information may be extracted from the nonlinear signals of complex systems by displaying them in multiple dimensions.^{4,5} An important challenge in the interpretation of four-wave mixing (FWM) signals is the isolation of spectral features corresponding to a given pathway of the density-matrix trajectory (Liouville space pathway). In molecules with well-resolved spectra, this can be accomplished by simply tuning the frequencies. More elaborate pulse-shaping techniques are required for highly congested spectra with overlapping lines.

Coherent-control techniques combined with laser pulse shaping have been used to drive quantum systems into a desired state.^{6–10} These techniques may be applied to manipulate excitons in multidimensional spectroscopy.^{11–14} Shaping the polarization state of the electric field provides a new dimension of control parameters.¹⁵ This has been demonstrated by Gerber and co-workers^{10,16,17} who introduced a polarization pulse shaper to control the amplitude, phase, and polarization state of different frequency components of complex pulse shapes. The huge parameter space available for pulse shaping includes the amplitude and phase of the electric fields and the polarization state of light (the degree of ellipticity and the orientation of the ellipses). Oron *et al.* had used the technique to eliminate the nonresonant background and selectively excite closely lying Raman modes in coherent anti-Stokes Raman spectroscopy (CARS).¹⁸ Multipolarization optimal control [two-dimensional (2D) and three-dimensional (3D)] has recently been applied to optimize the yield and access otherwise unattainable excited states.¹⁹ The influence of the elliptical polarization of the pump field on the evolution of electronic wave-packets and high-harmonic emission^{20,21} was used in polarization pulse shaping for the generation of attosecond pulses.²² First attempts have been

made towards shaping of attosecond pulses and their use in the control of strong-field atomic and molecular processes.²³ Adaptive control has been recently used for the generation of coherent soft x-rays.²⁴

FWM signals are associated with the third-order polarization which can be expressed using the time-dependent third-order response function $S^{(3)}$.¹ The system interacts with a sequence of laser pulses (Fig. 1), whose electric field is given by

$$\mathbf{E}(\mathbf{r}, \tau) = \sum_{j=1}^4 \sum_{\nu} A_{j\nu}(\tau - \bar{\tau}_j) \exp[i\mathbf{k}_j \cdot \mathbf{r} - i\bar{\omega}_j(\tau - \bar{\tau}_j) - i\varphi_{j\nu}(\tau - \bar{\tau}_j)] + \text{c.c.}, \quad (1)$$

where $A_{j\nu}(\tau - \bar{\tau}_j)$ is the slowly varying envelope function of pulse j polarized along the direction $\nu = x, y, z$ and centered at time $\bar{\tau}_j$ with carrier frequency $\bar{\omega}_j$, wave vector \mathbf{k}_j , and temporal phase function $\varphi_{j\nu}(\tau - \bar{\tau}_j)$.^{25,26} c.c. denotes the complex conjugate. Both A and φ are real functions.

In the frequency domain, the electric field is represented by

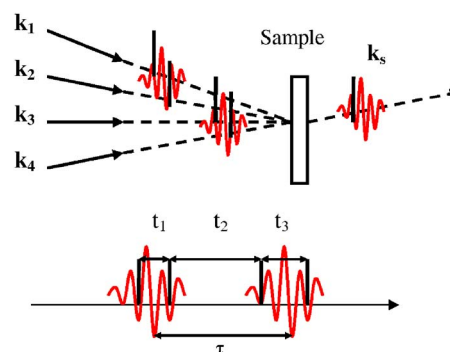


FIG. 1. Laser pulse sequence and time variables in a FWM experiment.

^{a)}Electronic mail: smukamel@uci.edu

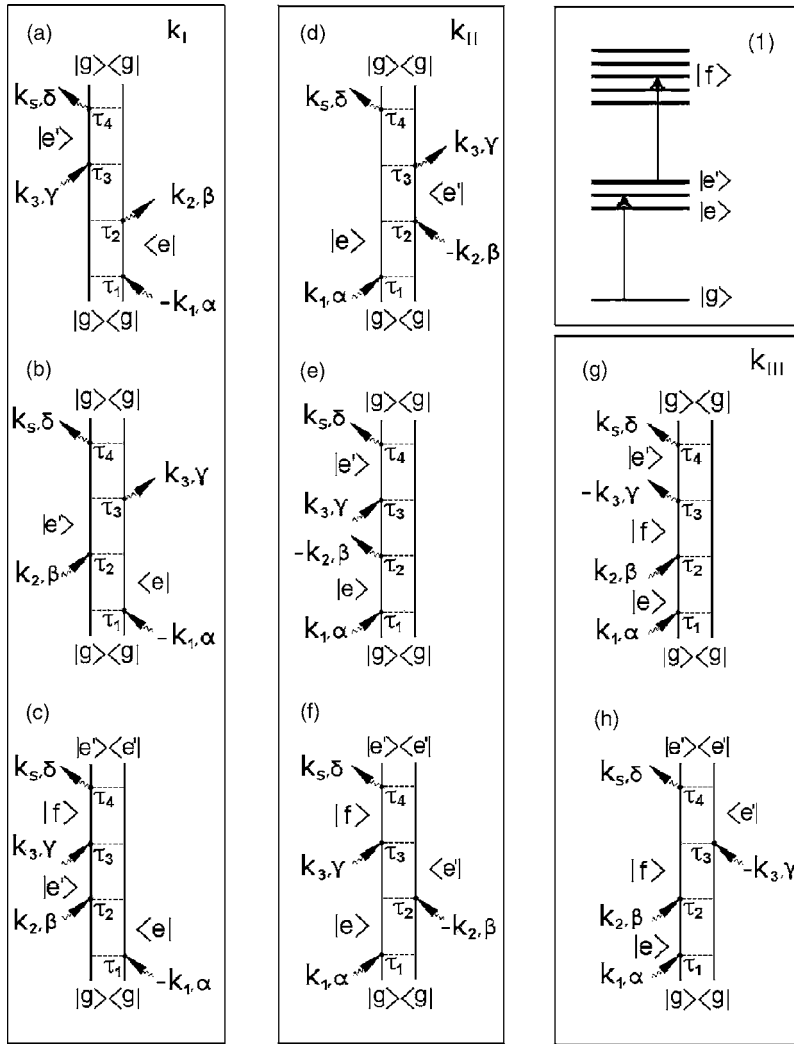


FIG. 2. Double-sided Feynman diagrams and Liouville space pathways contributing to FWM in an excitonic system within the RWA for the three possible directions: $k_I = -k_1 + k_2 + k_3$, $k_{II} = k_1 - k_2 + k_3$, and $k_{III} = k_1 + k_2 - k_3$ [Eqs. (26)–(28)]. The level scheme is shown in the top right panel. $|e\rangle$ and $|f\rangle$ denote the single- and the two-exciton manifolds, respectively. α, β, γ , and δ are the polarization components of the electric field. The following diagrams contribute to the sequential pump-probe spectrum [Eq. (29)]: (c) and (f) contribute to excited-state absorption (ESA), (b) and (d) to stimulated emission (SE), and (a) and (e) to ground-state bleaching (GSB).

$$E(\mathbf{r}, \omega) = \sum_{j=1}^4 \sum_{\nu} B_{j\nu}(\omega - \bar{\omega}_j) \exp[i\mathbf{k}_j \cdot \mathbf{r} + i(\omega - \bar{\omega}_j)\tau + i\phi_{j\nu}(\omega - \bar{\omega}_j)] + \text{c.c.}, \quad (2)$$

where $B_{j\nu}(\omega) \exp(i\phi_{j\nu}(\omega))$ is the Fourier transform of the complex envelope function $A_{j\nu}(\tau) \exp(-i\phi_{j\nu}(\tau))$. Both A and ϕ are real functions.

Three incident optical fields $j=1, 2, 3$ mix through their coupling with the system to generate a signal field with a carrier frequency $\bar{\omega}_s$, wave vector \mathbf{k}_s , and polarization δ , in one of the possible wave vectors $\mathbf{k}_s = \pm \mathbf{k}_1 \pm \mathbf{k}_2 \pm \mathbf{k}_3$. In the heterodyne detection mode a fourth laser pulse with $\mathbf{k}_4 = \mathbf{k}_s$ is mixed with the generated field, and the signal is finally given by

$$\begin{aligned} \mathcal{W}_\delta(\mathbf{k}_s) &= \sum_{\alpha, \beta, \gamma} \int_{-\infty}^{\infty} d\mathbf{r} \exp(-i\mathbf{k}_s \cdot \mathbf{r}) \\ &\times \int_{-\infty}^{\infty} d\tau_4 \int_{-\infty}^{\tau_4} d\tau_3 \int_{-\infty}^{\tau_3} d\tau_2 \int_{-\infty}^{\tau_2} d\tau_1 S_{\delta\gamma\beta\alpha}^{(3)}(\tau_4, \tau_3, \tau_2, \tau_1) \\ &\times E_\delta(\mathbf{r}, \tau_4) E_\gamma(\mathbf{r}, \tau_3) E_\beta(\mathbf{r}, \tau_2) E_\alpha(\mathbf{r}, \tau_1), \end{aligned} \quad (3)$$

where $\alpha, \beta, \gamma, \delta = x, y, z$ denote the polarizations of the

electric field $E_\nu(\mathbf{r}, \tau)$. τ_j are the interaction times at spatial points \mathbf{r} .

The third-order response function $S_{\delta\gamma\beta\alpha}^{(3)}$ contains various contributions leading to the induced polarization in each of the eight possible phase-matched directions $\mathbf{k}_s = \pm \mathbf{k}_1 \pm \mathbf{k}_2 \pm \mathbf{k}_3$ with the corresponding frequencies $\omega_s = \pm \omega_1 \pm \omega_2 \pm \omega_3$. These represent different spectroscopic techniques. Only the resonant terms in the response function are retained in the rotating wave approximation (RWA) where highly oscillatory nonresonant terms are neglected (see Fig. 2).

Generally, $S^{(3)}$ has 8×81 terms (8 Liouville space pathways and 81 tensor components). Each term further involves a fourfold summation over molecular eigenstates, and the nonlinear response has strong interferences among these numerous contributions. Another type of interference arises from the multiple integrations over pulse envelopes $E_\nu(\mathbf{r}, \tau)$ in Eq. (3). $\mathcal{W}_\delta(\mathbf{k}_s)$ is a coherent superposition of the various tensor components.

The effects of electric-field polarization on third-order measurements in isotropic quantum dot ensembles have been investigated by Scholes,²⁷ who demonstrated the control of various contributions by a combination of linearly and circularly polarized pulses. By switching the relative helicity of

the pump and probe pulses the ratios of the excited-state absorption (ESA) to the ground-state bleaching/stimulated emission (GSB/SE) were varied by a factor of 6. It is the goal of this paper to show how to simplify the coherent nonlinear signals of complex aggregates by controlling these interferences through shaping the electric-field envelopes of various polarizations.

Optimal control theory (OCT) searches for the desired electric-field pulse shapes $E_\nu(\mathbf{r}, \tau)$ by solving nonlinear functional equations.⁶ It has recently been applied to control the exciton dynamics in the Fenna-Matthews-Olson (FMO) complex (heptamer) of the photosynthetic antenna system of green bacteria,¹² and in a larger 96 chromophore system, the photosystem 1 (PS1) of *S. Elongatus*.¹³ The excitation energy was localized on one of the sites in the aggregate by varying the spectral and temporal profiles of linearly polarized laser pulses. Linearly polarized pulses and simple form of the spectral phase function were recently applied towards the control of the energy flow in the light-harvesting complex LH2.¹⁴

We study the influence of pure-phase-polarization pulse shaping, where we hold both the spectral and temporal intensity profiles fixed, on pump-probe spectra of a helical pentamer. The pump-probe (transient absorption) signal can be viewed as a self-heterodyne FWM. We simplify the spectra and control the composition of exciton wave packets by manipulating the contributions of Liouville space pathways with specific polarization directions. Coherent control with polarization pulse shaping is described in Sec. II. In Sec. III we introduce the exciton model and review the cumulant expansion of Gaussian fluctuation (CGF) expressions for the nonlinear-response functions for FWM. Simulations of sequential pump-probe spectra with well-separated pulses and the effect of phase-only polarization pulse shaping are presented in Sec. IV. The results are discussed in Sec. V.

II. ADAPTIVE PHASE CONTROL WITH POLARIZATION PULSE SHAPING

Polarization pulse shaping will be described in the slowly varying envelope approximation following the approach of Brixner *et al.*¹⁶ The time evolution of the electric-field vector within one optical cycle around time t may be represented by an ellipse (Fig. 3). A complete characterization of polarization-shaped laser pulses is provided by the quasi-3D representation based on specifying the temporal intensity $I_j(t)$, total phase $\varphi_j(t)$, orientation of the ellipse $\theta_j(t)$, and ellipticity $\varepsilon_j(t)$. We assume an electric field propagating along z [Eq. (1)] with two polarization components $\nu=x$ and y .

We define an angle $\chi_j(t) \in [0, \pi/2]$ as the ratio of the amplitudes $A_{j\nu}(t)$:

$$\chi_j(t) = \arctan \frac{A_{jy}(t)}{A_{jx}(t)}, \quad (4)$$

and a second angle $\delta_j(t) \in [-\pi, \pi]$ is the difference between the temporal phase modulations:

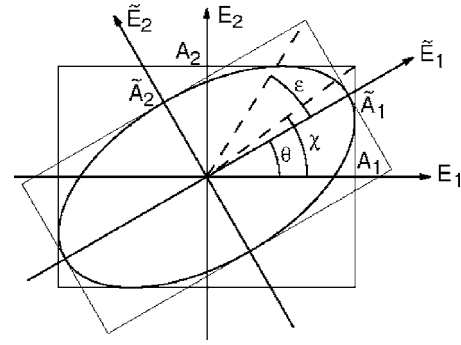


FIG. 3. Polarization ellipse representation of the electric field [adapted from Brixner (Ref. 28)]. \tilde{A}_1 and \tilde{A}_2 are the major and minor principle axes which define the angle of ellipticity ε (see Sec. II). The additional angles are the orientation angle of the ellipse θ and the auxiliary angle χ . The principal axes \tilde{A}_1 and \tilde{A}_2 are connected to the laboratory-frame amplitudes A_1 and A_2 by a principle-axis transformation. The polarization state of the laser pulses is defined by θ [Eq. (2)] and ε [Eq. (7)]. The sign of ε also defines the helicity: positive (negative) ε corresponds to the left (right) elliptically polarized light.

$$\delta_j(t) = \varphi_{jy}(t) - \varphi_{jx}(t). \quad (5)$$

$\tilde{\theta}_j(t) \in [-\pi/4, \pi/4]$ is a third angle,

$$\tilde{\theta}_j(t) = \frac{1}{2} \arctan[\tan(2\chi_j(t))\cos \delta_j(t)]. \quad (6)$$

The orientation angle of the ellipse $\theta_j(t) \in [-\pi/2, \pi/2]$ is then given by

$$\theta_j(t) = \begin{cases} \tilde{\theta}_j(t) & \text{if } \chi_j(t) \leq \pi/4 \\ \tilde{\theta}_j(t) + \pi/2 & \text{if } \chi_j(t) > \pi/4 \wedge \tilde{\theta}_j(t) < 0 \\ \tilde{\theta}_j(t) - \pi/2 & \text{if } \chi_j(t) > \pi/4 \wedge \tilde{\theta}_j(t) \geq 0. \end{cases}$$

The ellipticity angle $\varepsilon_j(t) \in [-\pi/4, \pi/4]$ is

$$\varepsilon_j(t) = \frac{1}{2} \arcsin[\sin(2\chi_j(t))\sin \delta_j(t)]. \quad (7)$$

Finally, the total phase $\varphi_j(t)$ of the laser-field oscillation with respect to the perihelion of the momentary light ellipse is defined as

$$\varphi_j(t) = \varphi_{jx}(t) + \text{sgn}[\theta_j(t)\varepsilon_j(t)] \times \arccos \left[\sqrt{\frac{I_j(t)}{[A_{jx}(t)]^2}} \cos \theta_j(t) \cos \varepsilon_j(t) \right]. \quad (8)$$

The instantaneous pulse frequency $\omega_j(t)$ is given by the time derivative of $\varphi_j(t)$,

$$\omega_j(t) = \bar{\omega}_j + \frac{d\varphi_j(t)}{dt}. \quad (9)$$

The elliptical electric-field parameters $\theta_j(t)$ and $\varepsilon_j(t)$ defined above can be displayed in a quasi-3D representation which provides a complete characterization of the complex polarization-shaped pulse. A set of instantaneous light ellipses is plotted at different times along the propagation axis of the electric field. The ellipse size represents the intensity and their shapes provide instantaneous snapshots of the polarization state. The shadows represent the intensities of individual electric-field components. The variation of the total phase (chirp) is shown by color.

The temporal and spectral amplitude profiles of the laser pulses are the primary features which determine the response. Using spectral phase shaping, Brixner *et al.* found that highly complex temporal field profiles were necessary for the optimization of the photodissociation of $\text{CpFe}(\text{CO})_2\text{Cl}$.¹⁰ In this paper we hold the total temporal and spectral amplitude profiles fixed and focus on the more subtle effects related to the polarization state of the pulse, which can have profound effects in chiral systems. The spectral amplitudes of both electric-field components $B_{j\nu}(\omega)$ and $I_j(\omega) \equiv B_{jx}^2(\omega) + B_{jy}^2(\omega)$ are kept fixed. We vary the temporal components $A_{jx}(t)$ and $A_{jy}(t)$ holding the total temporal intensity profile $I_j(t) \equiv A_{jx}^2(t) + A_{jy}^2(t)$ fixed.

The temporal $[\varphi_{j\nu}(t)]$ and spectral $[\phi_{j\nu}(\omega)]$ phases were calculated using the iterative Fourier transform algorithm (IFT).²⁹ This algorithm requires the initial spectral phase $\phi_{j\nu,0}(\omega)$, the fixed $B_{j\nu}(\omega)$, and the desired $A_{j\nu}(t)$ amplitude profiles as an input. First an inverse Fourier transform is applied to the field $\mathcal{E}_{j\nu,0}(\omega) = B_{j\nu}(\omega)\exp(-i\phi_{j\nu,0}(\omega))$: $B_{j\nu}(\omega)\exp(-i\phi_{j\nu,0}(\omega)) \Leftrightarrow a_{j\nu}(t)\exp(-i\varphi_{j\nu}(t))$. Then the amplitude $a_{j\nu}(t)$ is replaced by the target amplitude $A_{j\nu}(t)$ (time domain constraint) keeping the phase $\varphi_{j\nu}(t)$ unchanged: $\mathcal{E}_{j\nu,0}(t) = A_{j\nu}(t)\exp(-i\varphi_{j\nu}(t))$. A Fourier transform is then applied to $\mathcal{E}_{j\nu,0}(t)$: $A_{j\nu}(t)\exp(-i\varphi_{j\nu}(t)) \Leftrightarrow b_{j\nu}(\omega)\exp(-i\phi_{j\nu}(\omega))$ completing the first IFT loop. We integrated the areas under $A_{j\nu}(t)$ and used the integrals to rescale $B_{j\nu}(\omega)$. As a result the initial spectral phase $\phi_{j\nu,0}(\omega)$ is modified. $b_{j\nu}(\omega)$ is then replaced by $B_{j\nu}(\omega)$, and the procedure is repeated iteratively until convergence is achieved where $a_{j\nu}(t)$ is equal to $A_{j\nu}(t)$.

Using IFT we can hold the total intensity profiles $I_j(t)$ and $I_j(\omega)$ constant during the optimization process and vary only the temporal and spectral phases. To obtain $A_{j\nu}(t)$ we varied the auxiliary angle $\chi_j(t)$ (Fig. 3). Using Eq. (1) together with the constraints in Eq. (4) and keeping $I_j(t)$ fixed we then obtained the envelopes $A_{j\nu}(t)$.

Our search for the optimal parameters used the same genetic learning algorithm previously applied to multidimensional femtosecond spectroscopy of excitons.^{11,30} Briefly, it consists of several successive steps which, adopting evolution theory terminology, are labeled as population creation, selection, crossing, and mutation.³¹ In the population-creation step the first population of N laser pulses is created each with its own set of the initially predefined values of the optimization space parameters. In the selection step the cost function is calculated which represents the spectroscopic target of the coherent control. Then the selection of the best part of the population is made based on the parameters of the algorithm and the rest of the population is replenished by means of crossing. In order to explore the new points of the parameter space, mutation (noise) is added to all parameters of the newly created population.

The optimization process involves repeating the selection, crossing, and mutation sequence finally leading to an optimized population. To narrow down the range of populations in the optimal solution, the noise is reduced (or increased) depending on the average cost of the population on the previous step. The population is evaluated by defining the cost threshold W_{\max} and the number of population members N_{bad} with the cost *below* (for maximization) or *above* (for

minimization) W_{\max} . The decision is then made depending on the ratio $\eta = N_{\text{bad}}/N$. If $\eta \leq 0.5$ (population is “good”) the cost threshold is increased (reduced) by a factor of 2 (and the noise parameter σ_{mut} is increased by a factor of ϵ to escape possible local minima). For $\eta > 0.5$ the noise parameter σ_{mut} is reduced by the same factor ϵ , allowing to narrow the population distribution around the global minima.

III. FOUR-WAVE MIXING IN AGGREGATES

We describe an aggregate made of N interacting two-level molecules linearly coupled to a harmonic phonon bath by the Frenkel-exciton Hamiltonian:

$$\hat{H} = \hat{H}_S + \hat{H}_{\text{SF}} + \hat{H}_{\text{SB}}. \quad (10)$$

The three terms represent the isolated aggregate, the interaction with the optical field, and the interaction with a phonon bath, respectively. Exciton creation and annihilation operators of an excitation on the m th chromophore are given by \hat{B}_m^\dagger and \hat{B}_m and satisfy the Pauli commutation relations: $[\hat{B}_m, \hat{B}_n^\dagger] = \delta_{m,n}(1 - 2\hat{B}_n^\dagger\hat{B}_n)$. The system Hamiltonian is

$$\hat{H}_S = \sum_m \Omega_m \hat{B}_m^\dagger \hat{B}_m + \sum_{m \neq n} J_{mn} \hat{B}_m^\dagger \hat{B}_n, \quad (11)$$

where Ω_m is the excitation frequency of chromophore m and J_{mn} is the resonant nearest-neighbor exciton coupling in the Heitler-London approximation. The eigenstates relevant for the third-order response form three manifolds (Fig. 2): the ground state g , the N single excitons e and e' , and the $N(N-1)/2$ two-exciton states f .

The dipole interaction with the optical field $E(\mathbf{r}, \tau)$ within the RWA is

$$\begin{aligned} \hat{H}_{\text{SF}} = & - \sum_\nu \sum_j \sum_m [\mu_m^\nu \hat{B}_m^\dagger \mathcal{E}_{j\nu}(\tau) \exp(-i\bar{\omega}_j \tau) \\ & + \mu_m^\nu \hat{B}_m \mathcal{E}_{j\nu}^*(\tau) \exp(i\bar{\omega}_j \tau)], \end{aligned} \quad (12)$$

where $\mathcal{E}_{j\nu}(\tau) \equiv A_{j\nu}(\tau)\exp(-i\varphi_{j\nu}(\tau))$, and μ_m^ν is the ν th component of the transition dipole moment of the m th molecule.

$$\hat{H}_{\text{SB}} \equiv \sum_{\nu,n} q_\nu \bar{\Omega}_{n,\nu} \hat{B}_n^\dagger \hat{B}_n, \quad (13)$$

is the system-bath interaction where $\bar{\Omega}_{n,\nu}$ denote the coupling to the collective bath coordinate q_ν .³²

Only g to e and e to f transitions are allowed by Eq. (12). These eigenstates ψ_{an} are obtained by diagonalizing the one- and two-exciton blocks of the system Hamiltonian.³³

\hat{H}_{SB} introduces fluctuations into the Hamiltonian through the following collective coordinates defined in the eigenstate basis:

$$Q_{ab} = \sum_{mn,\nu} \psi_{am} \psi_{bn} q_\nu \bar{\Omega}_{n,\nu}, \quad (14)$$

where the sum runs over all molecules m and n and bath modes ν . We assume only diagonal interactions with the bath (Q_{aa}).

The linear absorption of this model is given by¹

$$S_{\text{la}}(\omega) = \sum_{\xi} \frac{2|\mu_{\xi}|^2 \Omega_{\xi}}{(\omega - \Omega_{\xi})^2 + \Gamma_{\xi}^2}, \quad (15)$$

where Γ_{ξ} is the electronic dephasing rate and μ_{ξ} is the transition dipole moment from the ground to the one-exciton state ξ with transition frequency Ω_{ξ} . These are obtained by diagonalizing \hat{H}_S .

The third-order response functions were obtained using the Cumulant expansion of Gaussian fluctuations (CGF) approach.³² The total response function $S_{\delta\gamma\beta\alpha}^{(3)}(\tau_4, \tau_3, \tau_2, \tau_1)$ which relates the third-order nonlinear polarization to the electric field [Eq. (3)] is given by a sum of eight Liouville space pathways:

$$\begin{aligned} S_{\delta\gamma\beta\alpha}^{(3)}(\tau_4, \tau_3, \tau_2, \tau_1) = & i^3 [\mathcal{F}_{\beta\gamma\delta\alpha}(\tau_2, \tau_3, \tau_4, \tau_1) \\ & + \mathcal{F}_{\alpha\gamma\delta\beta}(\tau_1, \tau_3, \tau_4, \tau_2) \\ & + \mathcal{F}_{\alpha\beta\delta\gamma}(\tau_1, \tau_2, \tau_4, \tau_3) \\ & + \mathcal{F}_{\delta\gamma\beta\alpha}(\tau_4, \tau_3, \tau_2, \tau_1)] + \text{c.c.} \end{aligned} \quad (16)$$

Here

$$\mathcal{F}_{\delta\gamma\beta\alpha}(\tau_4, \tau_3, \tau_2, \tau_1) = \hat{P}_{\delta}(\tau_4) \hat{P}_{\gamma}(\tau_3) \hat{P}_{\beta}(\tau_2) \hat{P}_{\alpha}(\tau_1) \quad (17)$$

is the four-point correlation function of the polarization operator with $\hat{P} = \sum_m \mu_m (\hat{B}_m^{\dagger} + \hat{B}_m)$ and

$(\hat{P}(\tau) = \exp(i\hat{H}_S\tau) \hat{P} \exp(-i\hat{H}_S\tau))$. Note the symmetry $\mathcal{F}_{\delta\gamma\beta\alpha}^*(\tau_4, \tau_3, \tau_2, \tau_1) = \mathcal{F}_{\alpha\beta\gamma\delta}(\tau_1, \tau_2, \tau_3, \tau_4)$.

For our model, the correlation function may be separated into two terms,

$$\begin{aligned} \mathcal{F}_{\delta\gamma\beta\alpha}(\tau_4, \tau_3, \tau_2, \tau_1) = & F_{\delta\gamma\beta\alpha}(\tau_4, \tau_3, \tau_2, \tau_1) \\ & + F'_{\delta\gamma\beta\alpha}(\tau_4, \tau_3, \tau_2, \tau_1), \end{aligned} \quad (18)$$

with

$$\begin{aligned} F_{\delta\gamma\beta\alpha}(\tau_4, \tau_3, \tau_2, \tau_1) = & \sum_{nmpq} \mu_q^{\delta} \mu_p^{\gamma} \mu_m^{\beta} \mu_n^{\alpha} \\ & \times \hat{B}_q(\tau_4) \hat{B}_p^{\dagger}(\tau_3) \hat{B}_m(\tau_2) \hat{B}_n^{\dagger}(\tau_1), \end{aligned} \quad (19)$$

and

$$\begin{aligned} F'_{\delta\gamma\beta\alpha}(\tau_4, \tau_3, \tau_2, \tau_1) = & \sum_{nmpq} \mu_q^{\delta} \mu_p^{\gamma} \mu_m^{\beta} \mu_n^{\alpha} \\ & \times \hat{B}_q(\tau_4) \hat{B}_p(\tau_3) \hat{B}_m^{\dagger}(\tau_2) \hat{B}_n^{\dagger}(\tau_1). \end{aligned} \quad (20)$$

These correlation functions may be evaluated using the second-order cumulant expansion.³² F only involves one-exciton states and is given by

$$F_{\delta\gamma\beta\alpha}(\tau_4, \tau_3, \tau_2, \tau_1) = \sum_{ee'} \mu_{ge'}^{\delta} \mu_{e'g}^{\gamma} \mu_{ge}^{\beta} \mu_{eg}^{\alpha} \exp[-i\Omega_{e'g}(\tau_4 - \tau_3) - i\Omega_{eg}(\tau_2 - \tau_1) - f(\tau_4, \tau_3, \tau_2, \tau_1)], \quad (21)$$

with

$$f(\tau_4, \tau_3, \tau_2, \tau_1) = g_{ee}(\tau_{21}) + g_{e'e'}(\tau_{43}) + g_{ee'}(\tau_{32}) + g_{ee'}(\tau_{41}) - g_{ee'}(\tau_{31}) - g_{ee'}(\tau_{42}), \quad (22)$$

F' contains two-exciton states and is given by

$$F'_{\delta\gamma\beta\alpha}(\tau_4, \tau_3, \tau_2, \tau_1) = \sum_{ee'f} \mu_{ge'}^{\delta} \mu_{e'f}^{\gamma} \mu_{fe}^{\beta} \mu_{eg}^{\alpha} \exp[i(-\Omega_{e'g}\tau_4 - \Omega_{fe'}\tau_3 + \Omega_{fe}\tau_2 + \Omega_{eg}\tau_1) - f'(\tau_4, \tau_3, \tau_2, \tau_1)], \quad (23)$$

with

$$\begin{aligned} f'(\tau_4, \tau_3, \tau_2, \tau_1) = & g_{ee}(\tau_{21}) + g_{ff}(\tau_{32}) + g_{e'e'}(\tau_{43}) - g_{ef}(\tau_{21}) \\ & - g_{ef}(\tau_{32}) + g_{ef}(\tau_{31}) + g_{ee'}(\tau_{32}) \\ & + g_{ee'}(\tau_{41}) - g_{ee'}(\tau_{31}) - g_{ee'}(\tau_{42}) \\ & - g_{fe'}(\tau_{32}) - g_{fe'}(\tau_{43}) + g_{fe'}(\tau_{42}), \end{aligned} \quad (24)$$

where $\tau_{ij} = \tau_i - \tau_j$. Ω_{ab} and μ_{ab} are transition frequencies and transition dipoles between states a and b .

The line-broadening functions $g_{ab}(t)$ are given by

$$\begin{aligned} g_{ab}(t) \equiv & \frac{1}{2} \int_0^t d\tau_1 \int_0^{\tau_1} d\tau_2 [\langle Q_{aa}(\tau_1) Q_{bb}(\tau_2) \rangle \\ & + \langle Q_{bb}(\tau_1) Q_{aa}(\tau_2) \rangle], \end{aligned} \quad (25)$$

where the collective coordinates Q_{aa} were defined in Eq. (14).

The possible FWM signals for our model are generated in the following three directions: $\mathbf{k}_I = -\mathbf{k}_1 + \mathbf{k}_2 + \mathbf{k}_3$, $\mathbf{k}_{II} = \mathbf{k}_1 - \mathbf{k}_2 + \mathbf{k}_3$, and $\mathbf{k}_{III} = \mathbf{k}_1 + \mathbf{k}_2 - \mathbf{k}_3$. Within the RWA the contributions to these techniques are represented by the double-sided Feynman diagrams (DFDs) shown in Fig. 2. Diagrams a, b , and c represent the three terms in Eq. (26), respectively. d, e , and f represent the three terms in Eq. (27), and g and h give the two terms in Eq. (28).

$$S_{\delta\gamma\beta\alpha}^{k_I}(\tau_4, \tau_3, \tau_2, \tau_1) = F_{\alpha\beta\delta\gamma}(\tau_1, \tau_2, \tau_4, \tau_3) + F_{\alpha\gamma\delta\beta}(\tau_1, \tau_3, \tau_4, \tau_2) - F'_{\alpha\delta\gamma\beta}(\tau_1, \tau_4, \tau_3, \tau_2), \quad (26)$$

$$S_{\delta\gamma\beta\alpha}^{k_{II}}(\tau_4, \tau_3, \tau_2, \tau_1) = F_{\beta\gamma\delta\alpha}(\tau_2, \tau_3, \tau_4, \tau_1) + F_{\delta\gamma\beta\alpha}(\tau_4, \tau_3, \tau_2, \tau_1) - F'_{\beta\delta\gamma\alpha}(\tau_2, \tau_4, \tau_3, \tau_1), \quad (27)$$

$$S_{\delta\gamma\beta\alpha}^{k_{III}}(\tau_4, \tau_3, \tau_2, \tau_1) = F'_{\delta\gamma\beta\alpha}(\tau_4, \tau_3, \tau_2, \tau_1) - F'_{\gamma\delta\beta\alpha}(\tau_3, \tau_4, \tau_2, \tau_1). \quad (28)$$

Equations (26)–(28) were used in our simulations.

IV. OPTIMIZED SEQUENTIAL PUMP-PROBE SPECTRA OF A HELICAL PENTAMER WITH POLARIZATION-SHAPED PULSES

Pump-probe is a self-heterodyne FWM technique. The system interacts with two light pulses, the pump and the probe, with wave vectors \mathbf{k}_1 and \mathbf{k}_2 and frequencies ω_1 and ω_2 , respectively. The signal is given by the difference of the probe absorption in the presence and in the absence of the pump and is observed in the direction $\mathbf{k}_s = \mathbf{k}_1 - \mathbf{k}_1 + \mathbf{k}_2 = \mathbf{k}_2$. The general expressions for heterodyne signals may be used by setting $\mathbf{k}_1 = \mathbf{k}_2$ for the pump and $\mathbf{k}_3 = \mathbf{k}_s$ for the probe. When the two pulses are temporally well separated, the system interacts first with the pump, and the resulting sequential pump-probe signal can be obtained from Eq. (3),¹

$$\begin{aligned} \mathcal{W}^{\text{PP}}(\omega_1, \omega_2; \tau) &= \sum_{\alpha} \mathcal{W}_{\alpha}^{\text{PP}} = \sum_{\alpha, \beta, \gamma, \delta} \Delta A_{\delta\gamma\beta\alpha} = \sum_{\alpha, \beta, \gamma, \delta} 2\omega_2 \text{Re} \int_{-\infty}^{\infty} d\tau_4 \int_{-\infty}^{\tau_4} d\tau_3 \int_{-\infty}^{\tau_3} d\tau_2 \int_{-\infty}^{\tau_2} d\tau_1 \\ &\times [\mathcal{E}_{2\delta}^*(\tau_4) \mathcal{E}_{2\gamma}(\tau_3) \mathcal{E}_{1\beta}^*(\tau_2) \mathcal{E}_{1\alpha}(\tau_1) S_{\delta\gamma\beta\alpha}^{k_{II}}(\tau_4, \tau_3, \tau_2, \tau_1) e^{i\omega_2\tau_4 + i\omega_1\tau_2} \\ &+ \mathcal{E}_{2\delta}^*(\tau_4) \mathcal{E}_{2\gamma}(\tau_3) \mathcal{E}_{1\beta}(\tau_2) \mathcal{E}_{1\alpha}^*(\tau_1) S_{\delta\gamma\beta\alpha}^{k_I}(\tau_4, \tau_3, \tau_2, \tau_1) e^{i\omega_2\tau_4 - i\omega_1\tau_2}], \end{aligned} \quad (29)$$

where $\tau_{ij} = \tau_i - \tau_j$ and S^{k_I} and $S^{k_{II}}$ are given by Eqs. (26) and (27).

Only six Feynman diagrams (Fig. 2) contribute to the pump-probe technique. These represent ESA [(c) and (f)], SE [(b) and (d)], and GSB [(a) and (e)].

Calculation of the pump-probe spectrum for shaped laser pulses of finite duration requires fourfold time integrations. Equation (29) may be recast in terms of the variables t_1, t_2 , and t_3 (Fig. 2) which represent the time intervals between successive interactions:

$$\begin{aligned} \mathcal{W}^{\text{PP}}(\omega_1, \omega_2; \tau) &= \sum_{\alpha, \beta, \gamma, \delta} 2\omega_2 \text{Re} \int_{-\infty}^{\infty} dt \int_0^{\infty} dt_3 \int_0^{\infty} dt_2 \int_0^{\infty} dt_1 \times [\mathcal{E}_{2\delta}^*(t) \mathcal{E}_{2\gamma}(t-t_3) \mathcal{E}_{1\beta}^*(t-t_3-t_2) \mathcal{E}_{1\alpha}(t-t_3-t_2-t_1) \\ &\times S_{\delta\gamma\beta\alpha}^{k_{II}}(t_3, t_2, t_1) e^{i\omega_2 t_3 + i\omega_1 t_1} + \mathcal{E}_{2\delta}^*(t) \mathcal{E}_{2\gamma}(t-t_3) \mathcal{E}_{1\beta}(t-t_3-t_2) \mathcal{E}_{1\alpha}^*(t-t_3-t_2-t_1) S_{\delta\gamma\beta\alpha}^{k_I}(t_3, t_2, t_1) e^{i\omega_2 t_3 - i\omega_1 t_1}]. \end{aligned} \quad (30)$$

For the simulation of isotropic ensembles we performed rotational averagings of the products of transition dipoles with respect to a laboratory frame using Eqs. (38) and (41) of Ref. 34. The only tensor components of the response function in an isotropic system are S_{xxxx} , S_{xyxy} , S_{xyyy} , and S_{xyyx} (+ identical terms where x and y are interchanged).

Circular molecular aggregates such as LH2,³⁵ helical aggregates,³⁶ and polypeptides^{37–39} are suitable candidates for polarization-sensitive optimization. Linear absorption of helical systems shows two absorption bands,^{40,41} a longitudinal band, polarized along the helical axis, and a transverse band (a combination of the degenerate transitions). In circular dichroism (CD) these bands have equal amplitudes and opposite signs. The ratio of the amplitudes of these bands varies with aggregate geometry.^{35,38}

Electronic and vibrational spectroscopic techniques have been widely applied to study structural fingerprints in the spectrum of helical peptides. Vibrational amide bands ($C=O$ stretches) in IR (Ref. 42–44) and $\pi-\pi^*$ with n

$-\pi^*$ transitions in UV (Ref. 45) are well resolved and sensitive to the peptide backbone configuration. The Frenkel exciton model is usually applied to such systems. A coupled three-level oscillator model is used for vibrational excitons, and a two-level oscillator model is used for electronic transitions.

We have applied phase-controlled polarization pulse shaping to the optical excitations of the helical pentamer shown in Fig. 4 (top). We assumed nearest-neighbor interactions $J=200 \text{ cm}^{-1}$ between monomers along the helix backbone. The transition dipole moments in the molecular local basis (μ_x, μ_y, μ_z) are $\mu_1=(1, 0, 0)$, $\mu_2=(\cos \theta, \sin \theta, 1)$, $\mu_3=(\cos 2\theta, \sin 2\theta, 2)$, $\mu_4=(\cos 3\theta, \sin 3\theta, 3)$, and $\mu_5=(\cos 4\theta, \sin 4\theta, 4)$ with the angle $\theta=2.513 \text{ rad}$.

In all calculations we used the Lorentzian model of the line-broadening function $g_{ab}(t)=\Gamma_{ab}t$, where $\Gamma_{ab}=\Gamma=100 \text{ cm}^{-1}$ is the same homogeneous dephasing rate of all transitions. Figure 4 (bottom) shows the linear absorption (dashed line). Shown also is a spectrum with $\Gamma=10 \text{ cm}^{-1}$

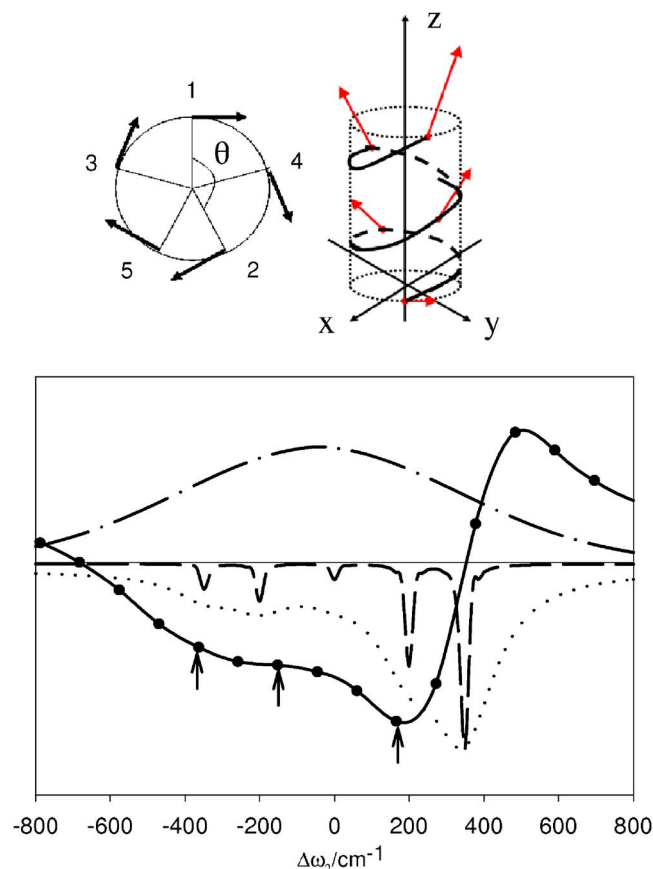


FIG. 4. Top: side view (left) and top view (right) of the helical pentamer. The angle $\Theta=2.513$ rad. Bottom: linear absorption spectrum $[-S_{l0}(\omega)]$ with the dephasing rate $\Gamma=10$ cm^{-1} (dashed line) and 100 cm^{-1} (dotted line); pump-probe spectrum with linearly polarized 117 fs FWHM pump and probe with $\Delta\omega_1=0$ cm^{-1} (solid line); and laser pulse (dot-dashed line). The arrows indicate the frequencies, $\Delta\omega_2=200, -150, -400$ cm^{-1} , used to define the optimization targets.

(solid line). $\Delta\omega=\omega-\omega_0$ is the detuning from the transition energy of the monomer. The spectrum shows stronger blue- and weaker redshifted transitions. The transition energies of the five one-exciton states and the corresponding normalized transition dipole moments are given in Table I. Transitions from the ground state to all five exciton states are allowed with the following order of the oscillator strengths: $5 > 4 > 2 > 1 > 3$. The system thus behaves like an H aggregate.

The pump-probe spectra were calculated using Eq. (30) for $\tau=1.5$ ps and dephasing time $\Gamma^{-1}=167$ fm. Pulse shaping was only applied to the pump. The probe was kept linearly polarized and was given by a sum of Gaussian x and y components with equal amplitudes. The quartuple time integrations were performed using the method of rectangles with the

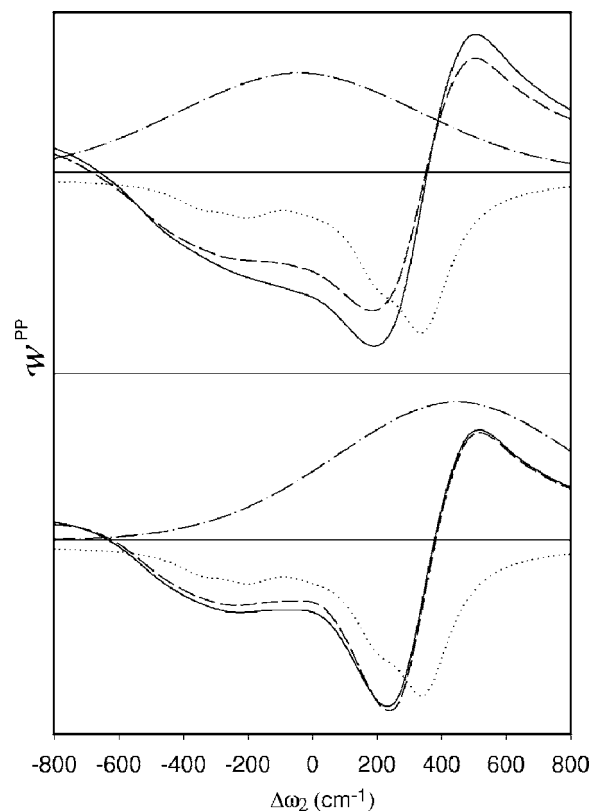


FIG. 5. Pump-probe spectra of the helical pentamer for $\tau=1.5$ ps: (top)—linearly polarized 117 fs FWHM pump laser pulse with $\Delta\omega_1=0$ with the polarization of the pump either parallel or perpendicular to that of the probe (both curves are equal and shown as a dashed line), and the similar spectrum induced by the circularly polarized pump and linearly polarized probe (solid line); (bottom)—spectra taken with the same parameters as above but with $\Delta\omega_1=500$ cm^{-1} , the spectrum obtained with linearly polarized pulses (dashed line) and with the circularly polarized pump (solid line). Linear ground-state absorption (dotted line) and the pump laser spectrum (dot-dashed line).

integration grid of 50 points in each dimension. The spectral profile of the pump had a Gaussian envelope $E_G(\omega)=1/(\sqrt{2\pi}\sigma_G)\exp(-(\omega-\bar{\omega})^2/2\sigma_G^2)$, where the carrier frequency $\bar{\omega}=\omega_0$ (and $\bar{\omega}=\omega_0+500$ cm^{-1}) and the spectral width $\sigma_G=311$ cm^{-1} were chosen to excite a wave packet of all the five one-exciton states. The temporal Gaussian profiles had a full width at half maximum (FWHM)= 117 fs obtained by applying a quadratic $\phi_{j\nu}(\omega)$ with IFT.

The calculated spectra for linearly and circularly polarized laser pulses are shown in Figs. 5 and 6. The linearly polarized spectra were identical when the pump polarization was parallel or perpendicular to the probe. Circularly polarized electric field is obtained by the application of the $\pi/2$

TABLE I. Exciton energies and transition dipoles for the helical pentamer shown in Fig. 4. $\mu_1=(\mu_x, \mu_y, \mu_z)=(1, 0, 0)$ is the transition dipole moment of monomer 1 in the local basis set.

	$\Delta\omega(\text{cm}^{-1})$	μ_x/μ_1	μ_y/μ_1	μ_z/μ_1	μ/μ_1
ξ_1	-346	0.483 543	-1.488 19	0.309 401	1.595 071
ξ_2	-200	1.463 53	0.475 528	-1	1.835 224
ξ_3	0	-0.068 15	0.209 735	1.154 7	1.175 570
ξ_4	200	0.345 492	0.112 257	-3	3.021 914
ξ_5	346	-0.016 46	0.050 649	4.309 4	4.309 729

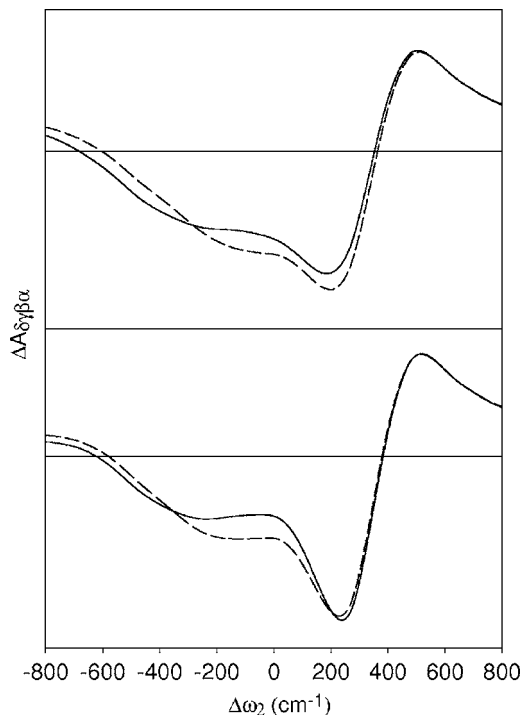


FIG. 6. Tensor components of the pump-probe spectra contributing to the circularly polarized pump with $\Delta\omega_1=0$ cm^{-1} (top) and $\Delta\omega_1=500$ cm^{-1} (bottom). ΔA_{xyyy} (solid line), $\Delta A_{xyyx}=\Delta A_{yyxx}$ (dashed line).

constant phase shift to the x component of the pump. The tensor components contributing to the circularly polarized spectra are shown in Fig. 6.

Our pump polarization shaping optimization started with both E_x and E_y components initially equal and with a Gaussian envelope $E_G(\tau)=\exp(-\tau^2/2\sigma_G^2)$ with FWHM=117 fs. We employed the genetic algorithm for the optimization of different spectral pump-probe features using 76 parameters of the search space grid with equally spaced points of the auxiliary angle $\chi_1(t)$ [see Eq. (4)]. The initial Gaussian profiles were modeled in a range of 600 fs using a 76-point grid. The distortion of the resulting pulse shapes due to numerical error of IFT was small and we were able to fit the total amplitude profile to a Gaussian to within a few percent.

We denote the detuning of pulse j with respect to $\Omega_m = \omega_0$ by $\Delta\omega_j = \omega_j - \omega_0$. Three cost functions were minimized, each controlling the ratio of the signal at two frequencies. (1) $W_1 = W^{PP}(\Delta\omega_2 = -150) / W^{PP}(\Delta\omega_2 = 200)$ with $\Delta\omega_1 = 0$. This maximizes the negative absorption peak at $\Delta\omega = 200$ cm^{-1} . (2) $W_2 = W^{PP}(\Delta\omega_2 = -150) / W^{PP}(\Delta\omega_2 = -400)$ with $\Delta\omega_1 = 0$ to maximize the unresolved peak at $\Delta\omega_2 = -400$ cm^{-1} . (3) $W_3 = W^{PP}(\Delta\omega_2 = -150) / W^{PP}(\Delta\omega_2 = 200)$ with $\Delta\omega_1 = 500$ cm^{-1} to maximize the peak at $\Delta\omega_2 = 200$ cm^{-1} . We shall denote the corresponding optimal pulses as P_1 , P_2 , and P_3 . The optimization trajectories of the cost functions are shown in Fig. 7. The average of the cost function distribution is an indication for convergence. At the end of the optimization, most points converge to the same value; however, there are points with large deviations which can be attributed to the limited precision of the IFT procedure. In all cases the convergence of the cost function was fast and took 10–20 generations. Optimal pulses were found already at the early stages of the optimi-

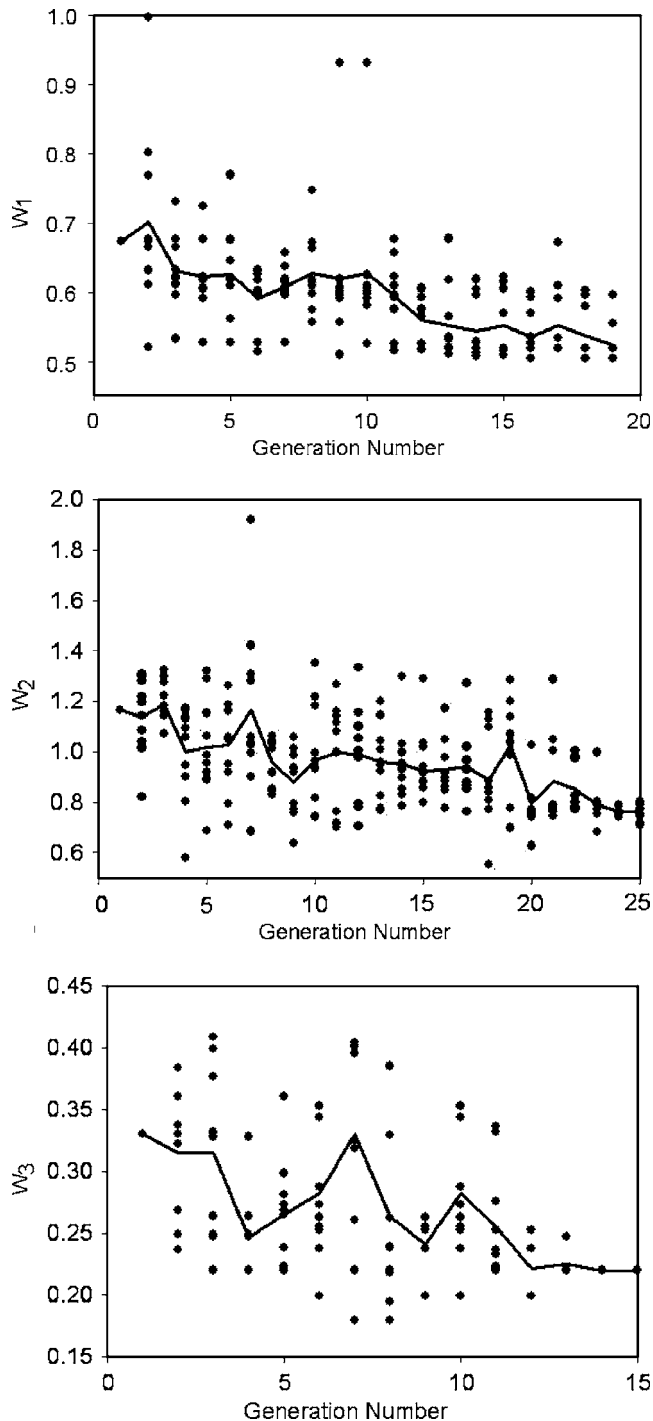


FIG. 7. Distribution of the cost function in the population of the genetic algorithm (circles) and its evolution during optimization of W_1 (top), W_2 (middle), and W_3 (bottom). The solid lines show the average cost values.

zation. This may be due to the low sensitivity of phase-only shaping or due to the existence of a large number of optimal or near-optimal pulses. W_1 was optimized by a factor of 1.2, and W_2 and W_3 by a factor of 2 compared to the Gaussian pulses.

The optimal pump-probe spectra for W_1 , W_2 , and W_3 are shown in Figs. 8(a)–8(c), respectively. The corresponding pump-probe tensor elements $\Delta A_{\alpha\beta\gamma\delta}$ [Eq. (29)] are given in Fig. 9. The quasi-three-dimensional representations of the optimized pulse shapes are displayed in Figs. 10 (P_1), 11

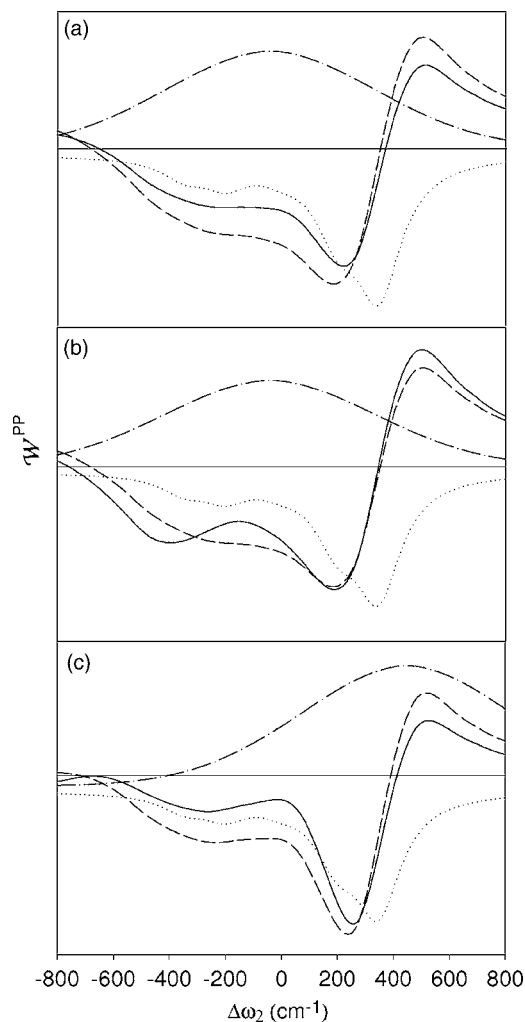


FIG. 8. Pump-probe spectra of the helical pentamer for $\tau=1.5$ ps with a polarization-shaped pump. (a) (Dashed line)—linearly polarized 117 fs FWHM pump with $\Delta\omega_1=0$ cm^{-1} ; (solid line)—the polarization-shaped pulse used for the optimization of the 200 cm^{-1} peak (P_1 , target W_1). Linear ground-state absorption spectrum is shown as a dotted line and the laser bandwidth is dash-dotted. (b) (Dashed line)—same as in (a); (solid line)—the polarization-shaped pulse for the optimization of the separation of the initially poorly resolved peaks at -400 and 200 cm^{-1} (P_2 , target W_2). Linear ground-state absorption spectrum is shown as a dotted line and the laser bandwidth is dash-dotted. (c) (Dashed line)—linearly polarized 117 fs FWHM pump with $\Delta\omega_1=500$ cm^{-1} ; (solid line)—polarization-shaped pulse used for the optimization of the 200 cm^{-1} peak (P_3 , target W_3). Linear ground-state absorption spectrum is shown as a dotted line and the pump laser bandwidth is shown as a dash-dotted line.

(P_2), and 12 (P_3). These pulses correspond to the minimum cost values of the last generation of the optimization (generations 19, 25, and 15 for P_1, P_2 , and P_3 , respectively). Elliptical parameters of these pulses (the temporal phases of the electric-field components $\varphi_{1,\nu}$) and parameters of the polarization state (the angles of the orientation of the ellipse θ_1 and ellipticity ε_1) are shown in Fig. 13. The phases determine the outcome of the convolution of the field polarization components with the relevant tensor components of the response function. The time-dependent phases of the polarization-shaped pulses are given in Fig. 14. This provides an alternative representation for the optimized laser pulses. Its time derivative yields the instantaneous pulse frequency presented in Figs. 10–12 using color scheme where

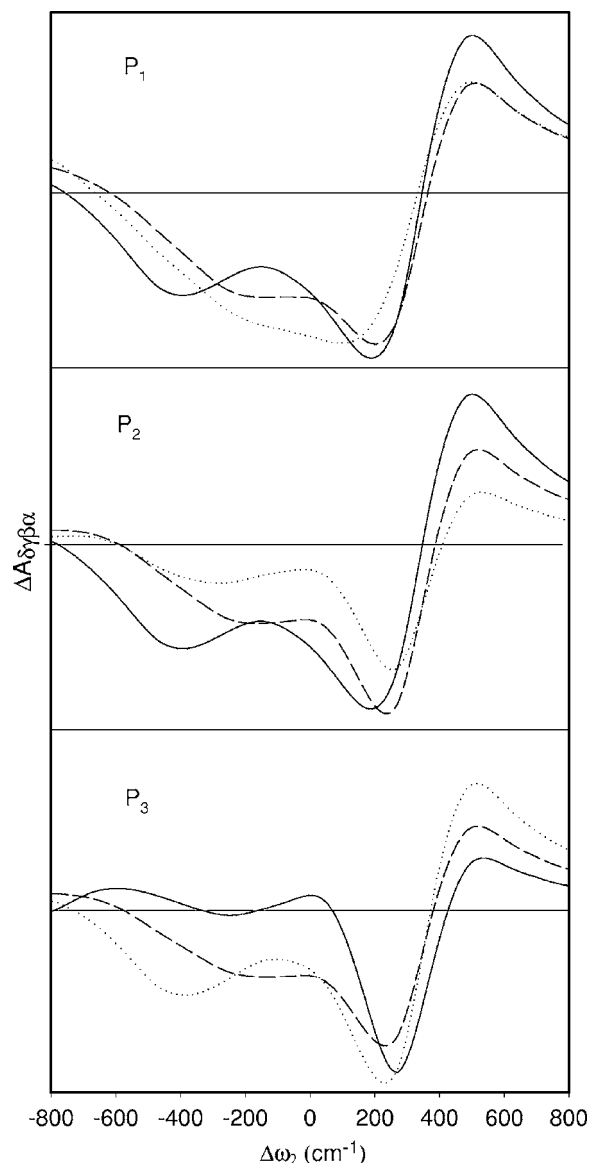


FIG. 9. Tensor components contributing to the pump-probe spectra for the optimized polarization-shaped laser pulses P_1, P_2 , and P_3 (top to bottom): (top)—tensor components $\Delta A_{xyxy} \times 2$ (dashed line), ΔA_{xxyy} (solid line), and $\Delta A_{xyyx} \times 2$ (dotted line); (middle)—tensor components ΔA_{xyxy} (dashed line), ΔA_{xxyy} (solid line), and ΔA_{xyyx} (dotted line); (bottom)—tensor components $\Delta A_{xyxy} \times 3$ (dashed line), $\Delta A_{xxyy} \times 3$ (solid line), and ΔA_{xyyx} (dotted line).

the monomer transition frequency is centered in blue with higher (lower) frequencies shown in violet (red).

The control target W_1 aims at isolating the blueshifted peak corresponding to the highest exciton state, minimizing the input of the lowest states [Fig. 8(a)]. The total pump-probe signal is given by a sum of several tensor elements [Eq. (29)]. These come from interactions with specific sequences of polarizations of the shaped electric-field components and represent contributions of different Liouville space pathways. Figure 9 (top) shows the component ΔA_{xyyx} with a new bleaching feature which can be attributed to the SE/GSB of the initially unresolved $n=3$ exciton state.

The optimized W_2 spectrum shown in Fig. 8(b) reveals a new redshifted peak (solid line). This is a combined contribution of GSB and SE from the lowest $n=1$ exciton state. The tensor elements for P_2 are shown in Fig. 9 (middle).

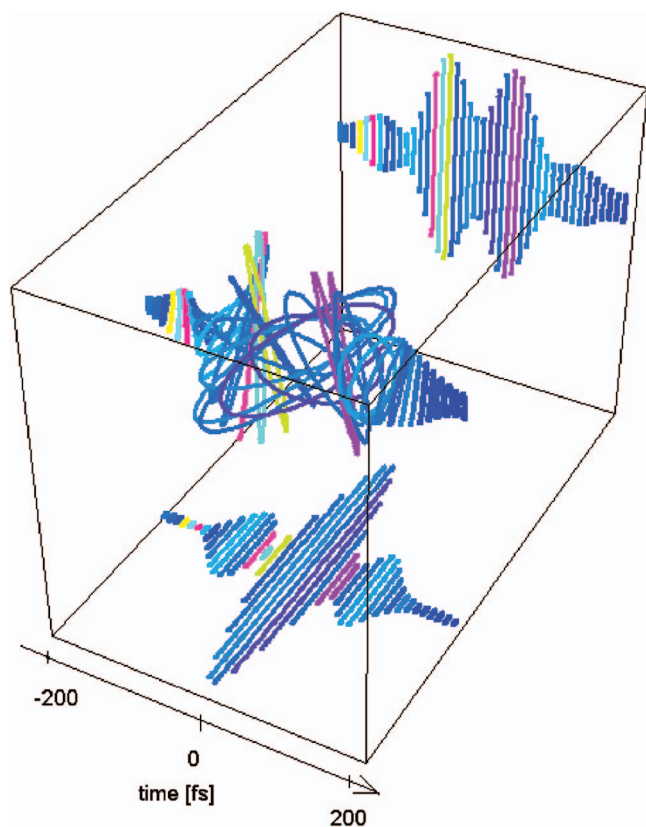


FIG. 10. (Color) Quasi-three-dimensional electric-field representation of the laser pulse P_1 in Fig. 8(a) (solid line). The instantaneous frequencies are indicated by colors with an arbitrary color scheme where light blue is chosen for the center frequency ω_0 . The projections to x (top) and y (bottom) axes represent the amplitude envelopes of the A_1 and A_2 components of the electric field.

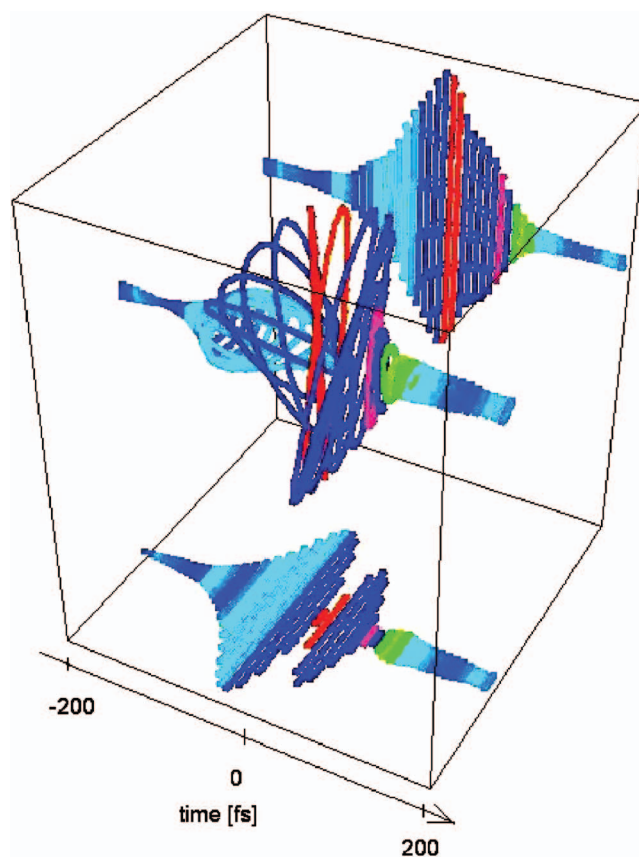


FIG. 11. (Color) Quasi-three-dimensional electric-field representation of the laser pulse P_2 in Fig. 8(b) (solid line) with the same parameters as in Fig. 10.

ΔA_{xxyy} is dominant. ΔA_{xyyx} contains a similar redshifted bleaching feature but also shows an ESA contribution.

The optimized W_3 spectrum [Fig. 8(c)] shows that the spectral shift of the pump carrier frequency leads to the partial removal of the lowest one-exciton states from the exciton wave packet. A new tensor element appears which contains the larger contribution from higher exciton states. The positive absorption peak at $\Delta\omega_2 = -600 \text{ cm}^{-1}$ can be assigned to the one- to two-exciton transition with the inter-ring character based on the analogy with the recent results on cylindrical aggregates.⁴⁶ The corresponding tensors are given in Fig. 9 (bottom).

The new peak in Fig. 8(b) is related to the SE/ESA contributions dominated by the ΔA_{xxyy} component [Fig. 9 (middle)]. Thus two successive interactions with either the x or y component of the pump are responsible for this effect. The corresponding phase variations of these components shown in Fig. 13 (P_2) can provide more information than the total phase profiles of Fig. 14. Our simulations were carried out on rotationally averaged ensembles and thus both the $\Delta A_{xxyy} = \Delta A_{yyxx}$ components contain the contributions of x - and y -polarized electric fields. It may be possible to further disentangle these contributions by using oriented ensembles.⁴⁷

As can be seen in Fig. 9 (bottom) ΔA_{xyyx} mainly includes the contributions from the SE and GSB from state $n=4$ and

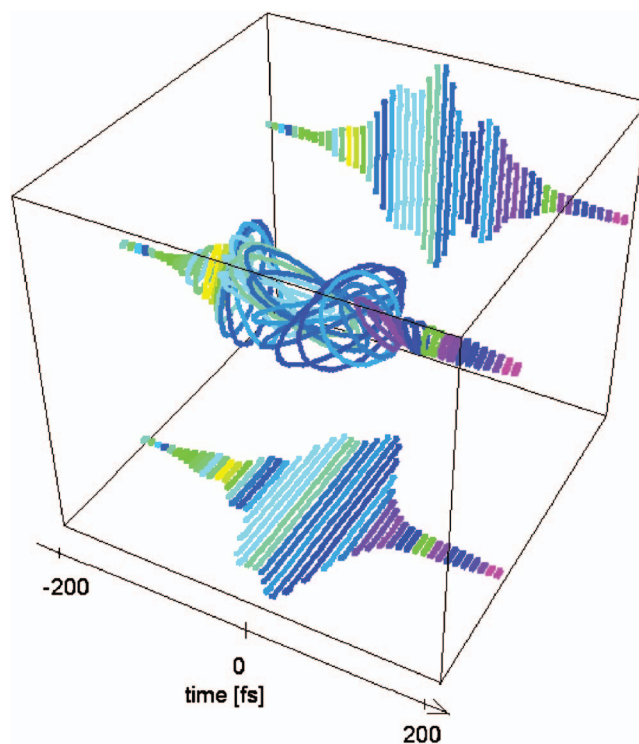


FIG. 12. (Color) Quasi-three-dimensional electric-field representation of the laser pulse P_3 in Fig. 8(c) (solid line) with the same parameters as in Fig. 10.

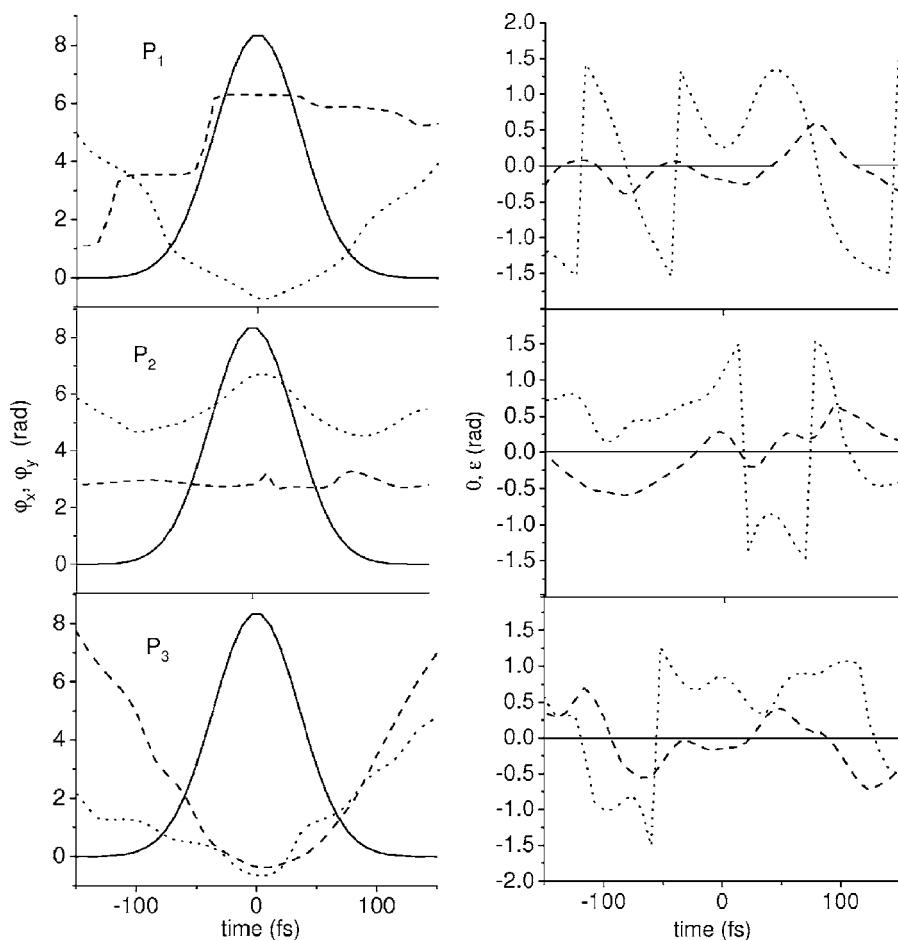


FIG. 13. Left: optimized time-dependent phase profiles $\varphi_x(t)$ (dashed line), $\varphi_y(t)$ (dotted line). Right: optimized elliptical parameters $\theta(t)$ (dotted line), $\varepsilon(t)$ (dashed line) for P_1 , P_2 , and P_3 .

the ESA from $n=5$ (Fig. 2). Modulations of the phases of the electric-field components φ_{1x} and φ_{1y} induce almost complete cancellation of the response from diagrams (b), (c), (d), and (f) for the state $n=4$ with diagrams (a) and (e) for $n=5$ accompanied by the slight narrowing of the remaining absorption and bleaching peaks.

The three-dimensional pulse shapes are shown in Figs. 10–12. P_2 and P_3 show significant modulations of the instantaneous frequency in the middle and at the end of the pulse duration. P_1 , on the other hand, is characterized by fast changes in the orientation angle and the degree of ellipticity.

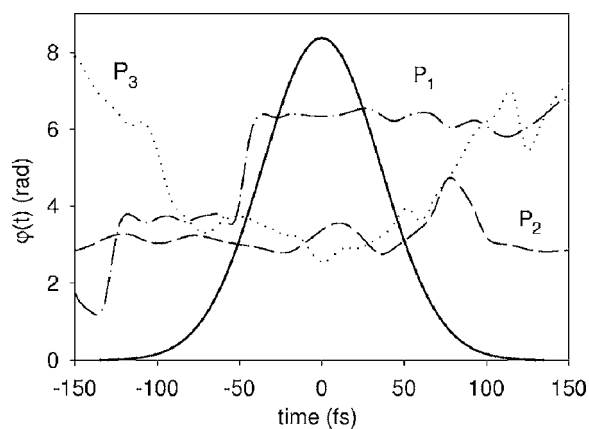


FIG. 14. Time dependence of the total phase $\varphi(t)$ [Eq. (8)] of the optimized laser pulses for P_1 , P_2 , and P_3 .

V. DISCUSSION

We have demonstrated the effect of polarization-shaped laser pulses on the ratios of two peaks in the pump-probe spectrum of excitons in a helical pentamer. The optimized electric fields select different Liouville space pathways of the tensor components of the response functions, highlighting several pump-probe tensor elements with distinct features. All tensor elements add coherently and interfere to obtain the pump-probe signal. A genetic algorithm was used to search for the optimized polarization-shaped laser pulses by modulating the E_x and E_y electric-field components. New peaks can be resolved and some peaks are suppressed in an otherwise poorly resolved spectrum.

Our calculations were made in the dipole approximation where there are only three linearly independent components for isotropic systems: $xyxy$, $xyyx$, and $xyyx$ ($xxxx$ is a linear combination of these components).⁴⁸ The signal propagation direction is determined by phase matching. These components have been used for improving of spectral resolution in 2D IR spectroscopies.^{49–53} Polarization shaping generates combinations of the three tensor components which amplify specific spectral features. Additional six chirally sensitive tensor components appear when the response function is expanded to first order in wave vector.³⁴

Further control of the spectroscopic targets may be achieved by varying other parameters such as the spectral and temporal laser envelopes.

Combination of different polarization components is utilized in CD, a linear technique, which measures the difference in absorption of left- and right-handed circularly polarized light.^{45,54–56} This is the simplest example of a wave-vector-induced signal and is related to the $S_{xy}^{(1)}$ elements of the linear-response tensor (when the field propagates along z). The technique is widely used for protein structure determination both in the UV (180–220 nm) and the IR (1000–3500 cm^{-1}).^{57–61} Pattern-recognition and decomposition algorithms have been used to distinguish between α -helical and β -sheet formations using electronic^{62–64} and vibrational CD.⁶⁵ We have recently showed that tensor components of the third-order response tensor expanded to first order in wave vector (beyond the dipole approximation) are induced by molecular chirality (have opposite signs for the mirror image of structure) and therefore are very promising in the studies of polarization-controlled spectroscopy.³⁴ Their dependence on the four optical wave vectors brings additional 12 parameters. The control of these parameters for chiral systems such as helical structures is an interesting direction for a future study.

ACKNOWLEDGMENTS

The support of Chemical Sciences, Geosciences and Biosciences Division, Office of Basic Energy Sciences, Office of Science, and U.S. Department of Energy is gratefully acknowledged. We also thank Dr. T. C. Jansen, Dr. J. Madox, and D. Healion for helpful discussions.

- ¹ S. Mukamel, *Principles of Nonlinear Optical Spectroscopy* (Oxford University Press, New York, 1995).
- ² *Ultrafast Phenomena IV*, edited by T. Kobayashi, T. Okada, T. Kobayashi, K. Nelson, and S. De Silvestri (Springer, New York, 2005).
- ³ T. Brixner, J. Stenger, H. Vaswani, M. Cho, R. Blankenship, and G. Fleming, *Nature* (London) **434**, 625 (2004).
- ⁴ S. Mukamel, *Annu. Rev. Phys. Chem.* **51**, 691 (2000).
- ⁵ Y. Tanimura and S. Mukamel, *J. Chem. Phys.* **99**, 9496 (1993).
- ⁶ S. Rice and M. Zhao, *Optical Control of Molecular Dynamics* (Wiley, New York, 2000).
- ⁷ M. Shapiro and P. Brumer, *Principles of the Quantum Control of Molecular Processes* (Wiley, Hoboken, NJ, 2003).
- ⁸ W. Warren, H. Rabitz, and M. Dahleh, *Science* **259**, 1581 (1993).
- ⁹ H. Rabitz, *Science* **299**, 525 (2003).
- ¹⁰ T. Brixner, B. Kiefer, and G. Gerber, *Chem. Phys.* **267**, 241 (2001).
- ¹¹ D. Abramavicius and S. Mukamel, *J. Chem. Phys.* **120**, 8373 (2004).
- ¹² B. Brueggemann and V. May, *J. Phys. Chem. B* **108**, 10529 (2004).
- ¹³ B. Brueggemann and V. May, *Chem. Phys. Lett.* **400**, 573 (2004).
- ¹⁴ W. Wohlleben, T. Buckup, J. L. Herek, and M. Motzkus, *ChemPhysChem* **6**, 850 (2005).
- ¹⁵ Y. Silberberg, *Nature* (London) **430**, 624 (2004).
- ¹⁶ T. Brixner, G. Krampert, P. Niklaus, and G. Gerber, *Appl. Phys. B: Lasers Opt.* **74**, S133 (2002).
- ¹⁷ T. Brixner, N. Damrauer, G. Krampert, P. Niklaus, and G. Gerber, *J. Opt. Soc. Am. B* **20**, 878 (2003).
- ¹⁸ D. Oron, N. Dudovich, and Y. Silberberg, *Phys. Rev. Lett.* **90**, 213902 (2003).
- ¹⁹ R. Wu, I. R. Sola, and H. Rabitz, *Chem. Phys. Lett.* **400**, 469 (2004).
- ²⁰ P. Dietrich, N. Burnett, M. Ivanov, and P. Corkum, *Phys. Rev. A* **50**, R3585 (1994).
- ²¹ K. Budil, P. Salieres, A. L'Huillier, T. Ditmire, and M. Perry, *Phys. Rev. A* **48**, R3437 (1993).

- ²² P. Corkum, N. Burnett, and M. Ivanov, *Opt. Lett.* **19**, 1870 (1994).
- ²³ J. Itatani, D. Zeidler, J. Levesque, M. Spanner, D. Villeneuve, and P. Corkum, *Phys. Rev. Lett.* **94**, 123902 (2005).
- ²⁴ T. Pfeifer, D. Walter, C. Winterfeldt, C. Spielmann, and G. Gerber, *Springer Ser. Chem. Phys.* **79**, 178 (2005).
- ²⁵ A. Albrecht, J. Hybl, S. Faeder, and D. Jonas, *J. Chem. Phys.* **111**, 10934 (1999).
- ²⁶ W. Zhang, V. Chernyak, and S. Mukamel, *J. Chem. Phys.* **110**, 5011 (1999).
- ²⁷ G. Scholes, *J. Chem. Phys.* **121**, 101104 (2004).
- ²⁸ T. Brixner, *Appl. Phys. B: Lasers Opt.* **76**, 531 (2003).
- ²⁹ M. Hacker, G. Stobrawa, and T. Feurer, *Opt. Lett.* **9**, 191 (2001).
- ³⁰ D. Zeidler, S. Frey, K.-L. Kompa, and M. Motzkus, *Phys. Rev. A* **64**, 023420 (2001).
- ³¹ D. E. Goldberg, *Genetic Algorithms in Search, Optimization, and Machine Learning* (Addison-Wesley, Reading, 1989).
- ³² S. Mukamel and D. Abramavicius, *Chem. Rev. (Washington, D.C.)* **104**, 2073 (2004).
- ³³ H. van Amerongen, L. Valkunas, and R. van Grondelle, *Photosynthetic Excitons* (World Scientific, Singapore, 2000).
- ³⁴ D. Abramavicius and S. Mukamel, *J. Chem. Phys.* **122**, 1 (2005).
- ³⁵ S. Georgakopoulou, R. Frese, E. Johnson, C. Koolhaas, R. Cogdell, R. van Grondelle, and G. van der Zwan, *Biophys. J.* **82**, 2184 (2002).
- ³⁶ C. Didruga, J. Klugkist, and J. Knoester, *J. Phys. Chem. B* **106**, 11474 (2002).
- ³⁷ R. Woody and A. Koslowski, *Biophys. Chem.* **101**, 535 (2002).
- ³⁸ R. Woody, *Eur. Biophys. J.* **23**, 253 (1994).
- ³⁹ R. Woody and N. Sreerama, *J. Chem. Phys.* **111**, 2844 (1999).
- ⁴⁰ W. Moffitt, *J. Chem. Phys.* **25**, 467 (1956).
- ⁴¹ W. Moffitt, *Proc. Natl. Acad. Sci. U.S.A.* **42**, 736 (1956).
- ⁴² S. Mukamel, *Annu. Rev. Phys. Chem.* **51**, 691 (2000).
- ⁴³ P. Hamm, M. Lim, and R. Hochstrasser, *J. Phys. Chem. B* **102**, 6123 (1998).
- ⁴⁴ M. Zanni and R. Hochstrasser, *Curr. Opin. Struct. Biol.* **11**, 516 (2001).
- ⁴⁵ *Circular Dichroism. Principles and Applications*, edited by N. Berova, K. Nakanishi, and R. W. Woody, 2nd ed. (Wiley, New York, 2000).
- ⁴⁶ M. Bednarz and J. Knoester, *J. Phys. Chem. B* **105**, 12913 (2001).
- ⁴⁷ D. Abramavicius, W. Zhuang, and S. Mukamel, *J. Phys. Chem. B* **108**, 18034 (2004).
- ⁴⁸ D. L. Andrews and T. Thirunamachandran, *J. Chem. Phys.* **67**, 5026 (1977).
- ⁴⁹ R. M. Hochstrasser, *Chem. Phys.* **266**, 273 (2001).
- ⁵⁰ M. T. Zanni, N.-H. Ge, Y. S. Kim, and R. M. Hochstrasser, *Proc. Natl. Acad. Sci. U.S.A.* **98**, 11265 (2001).
- ⁵¹ O. Golonzka and A. Tokmakoff, *J. Chem. Phys.* **115**, 297 (2001).
- ⁵² E. C. Fulmer, P. Mukherjee, A. T. Krummel, and M. T. Zanni, *J. Chem. Phys.* **120**, 8067 (2004).
- ⁵³ J. Dreyer, A. M. Moran, and S. Mukamel, *Bull. Korean Chem. Soc.* **24**, 1091 (2003).
- ⁵⁴ A. Moscovitz, *Adv. Chem. Phys.* **4**, 67 (1962).
- ⁵⁵ I. Tinoco, *Adv. Chem. Phys.* **4**, 113 (1962).
- ⁵⁶ L. D. Barron, *Molecular Light Scattering and Optical Activity*, 2nd ed. (Cambridge University Press, Cambridge, London, 2004).
- ⁵⁷ T. B. Freedman and L. A. Nafie, in *Modern Nonlinear Optics*, edited by M. Evans and S. Kielich (Wiley, New York, 1994), Pt. 3, p. 207.
- ⁵⁸ J. R. Cheesema, M. J. Frisch, F. J. Devlin, and P. J. Stephens, *Chem. Phys. Lett.* **252**, 211 (1996).
- ⁵⁹ P. J. Stephens, C. S. Ashvar, F. J. Devlin, J. R. Cheesema, and M. J. Frisch, *Mol. Phys.* **89**, 579 (1996).
- ⁶⁰ P. Bour, J. Sopkova, L. Bednarova, P. Malon, and T. A. Keiderling, *J. Comput. Chem.* **18**, 646 (1997).
- ⁶¹ P. J. Stephens and F. J. Devlin, *Chirality* **12**, 172 (2000).
- ⁶² N. Sreerama, S. Y. Venyaminov, and R. W. Woody, *Protein Sci.* **8**, 370 (1999).
- ⁶³ N. Sreerama, R. W. Venyaminov, and S. Y. Woody, *Anal. Biochem.* **287**, 243 (2000).
- ⁶⁴ N. Sreerama and R. W. Woody, *Anal. Biochem.* **287**, 252 (2000).
- ⁶⁵ V. Baumruk, P. Pancoska, and T. A. Keiderling, *J. Mol. Biol.* **259**, 774 (1996).